

First-principles studies on the dynamic, mechanical, and electronic properties of $ZrCr_2Hx$ ($0 < x \leq 4$) under 0-20 Gpa

Wenhui Zhang(张文慧) and Hui Wang(王晖)

Citation: Chin. Phys. B, 2026, 35 (**5**): 057101. DOI: 10.1088/1674-1056/ae0893
http://cpb.iphy.ac.cn; http://iopscience.iop.org/cpb

What follows is a list of articles you may be interested in

First-principles study of the bandgap renormalization and optical property of β-$LiGaO_2$

Dangqi Fang(方党旗)
Chin. Phys. B, 2023, 32 (**4**): 047101. DOI: 10.1088/1674-1056/acb9ef

Topological properties of Sb(111) surface: A first-principles study

Shuangxi Wang(王双喜) and Ping Zhang(张平)
Chin. Phys. B, 2022, 31 (**4**): 047105. DOI: 10.1088/1674-1056/ac46bc

First-principles study on improvement of two-dimensional hole gas concentration and confinement in AlN/GaN superlattices

Huihui He(何慧卉) and Shenyuan Yang(杨身园)
Chin. Phys. B, 2022, 31 (**1**): 017104. DOI: 10.1088/1674-1056/ac00a0

First-principles study of electronic structure and magnetic properties of $Sr_3Fe_2O_5$ oxide

Mavlanjan Rahman(买吾兰江·热合曼) and Jiuyang He(何久洋)
Chin. Phys. B, 2021, 30 (**11**): 117107. DOI: 10.1088/1674-1056/abfa06

First-principles calculations of F-, Cl-, and N-related defects of amorphous SiO_2 and their impacts on carrier trapping and proton release

Xin Gao(高鑫), Yunliang Yue(乐云亮), Yang Liu(刘杨), and Xu Zuo(左旭)
Chin. Phys. B, 2021, 30 (**4**): 047104. DOI: 10.1088/1674-1056/abe3f7

SPECIAL TOPIC — John Tse: Pioneer in high-pressure materials science

First-principles studies on the dynamic, mechanical, and electronic properties of $ZrCr_2H_x$ ($0 < x \leq 4$) under 0–20 GPa

Wenhui Zhang(张文慧) and Hui Wang(王晖)†

Key Laboratory for Photonic and Electronic Bandgap Materials (Ministry of Education), School of Physics and Electronic Engineering, Harbin Normal University, Harbin 150025, *China*

(Received 1 July 2025; revised manuscript received 8 September 2025; accepted manuscript online 18 September 2025)

Ternary metal hydrides play a vital role in the search for conventional high-temperature superconductors under near-ambient pressures. In this study, we examine the dynamic, mechanical, and electronic properties of the C15-type $ZrCr_2H_x$ ($0 < x \leq 4$) compounds at 0–20 GPa using first-principles simulations. We find that protons diffuse predominantly via the interstitial network composed of *g* and *e* sites, avoiding high-barrier *b* sites. Proton diffusion is insignificant at 300 K, but increases markedly with increasing temperature, leading to superionic transitions at 900 K in all these hydrides. Diffusion enhances the occupation probability of neighboring interstitial sites, resulting in short H–H separations that violate the Switendick criterion. The calculated thermoelastic properties indicate mechanical stability of $ZrCr_2H_x$ at room temperature. In $ZrCr_2H_4$, the high hydrogen concentration leads to a clear contribution of H *s* orbitals to metallicity, suggesting that C15-type intermetallic hydrides have great potential to form high-temperature superconductors at low pressures.

Keywords: metal hydrides, proton diffusion, superionic, first-principles study

PACS: 71.20.Lp, 66.30.–h, 62.20.–x, 71.15.Pd

DOI: 10.1088/1674-1056/ae0893 **CSTR:** 32038.14.CPB.ae0893

1. Introduction

Metal hydride research has emerged as a thriving frontier in high-pressure physics, driven by the experimental discovery of 250 K superconductivity in $LaH_{9.6}$ in 2019.[1,2] Over the past few years, dozens of superconducting hydrides have been identified under extreme pressures ranging from tens to hundreds of gigapascals, with critical temperatures (T_c) spanning a broad spectrum from millikelvin regimes to near-room-temperature conditions.[3–7] Current research priorities now focus on theoretical and experimental investigations of metal hydrides with tailored crystallographic structure, targeting the stabilization of superconducting phases at near-ambient conditions through compositional optimization strategies.[8–11]

Metal hydrides typically feature hydrogen atoms occupying interstitial sites within the host metallic lattice, which may comprise elemental metals, multicomponent alloys, or intermetallic compounds.[12] For superconducting metal hydrides, the extensive research has revealed remarkable structural diversity in these host lattices, encompassing prototype crystal systems such as face-centered cubic (fcc, *Fm*-3*m* space group), hexagonal close-packed (hcp, $P6_3/mmc$), and body-centered cubic (bcc, *Im*-3*m*) configurations. Recent theoretical and experimental investigations have demonstrated that ternary hydride systems exhibit superior capabilities in stabilizing superconducting phases under reduced pressure regimes compared to their binary counterparts.[13–17] A paradigmatic example emerges from the partial substitution of La atoms by Ce in the La–H system, which achieves a 43% reduction in stabilization pressure (from 170 GPa to 97 GPa) while maintaining superconducting T_c above 100 K.[18,19]

The C15-type intermetallic hydrides have attracted significant research attention due to their exceptional structural stability and hydrogen storage capacity.[20,21] Theoretical simulations show that 'C15-type' $MgLi_2H_{16}$ exhibits extraordinary superconducting performance, reaching a critical temperature of 400 K under 300 GPa. Experimental study of $ZrV_2H_{4-\delta}$ reveals ultrashort H–H distances of 1.6 Å at near-ambient conditions, directly challenging the Switendick criterion (minimum H–H separation $\geq$ 2.1 Å, proposed by Switendick in 1979)[22,23] that has historically governed metal hydride chemistry.[24] These findings stimulate further investigations into 'C15-type' ternary hydrides.

In Zr-based AB_2-type compounds with C15 structure, Zr is typically in the A site and acts as the "hydride forming" element, while the B site can be occupied by various elements, e.g., V, Mn, Cr, Fe, and Ni, which play a catalytic role in hydride formation.[25,26] With a high hydrogen capacity of up to 4 hydrogen atoms per formula unit, e.g. ZrV_2H_4 and $ZrCrH_4$, this class of compounds show a high potential to be developed into hydrogen-rich superconductors, and therefore it is interesting to further explore their dynamical, mechanical, and electronic properties at ambient and low pressures.

In this work, we study proton dynamics, elasticity, and

†Corresponding author. E-mail: wh@fysik.cn

© 2026 Chinese Physical Society and IOP Publishing Ltd. All rights, including for text and data mining, AI training, and similar technologies, are reserved.

electronic structures of $ZrCr_2H_x$ ($x = 0.125$, 1, 2, 4) at pressures of 0 GPa to 20 GPa and temperatures up to 1100 K by first-principles calculations. We find that the proton diffusivity depends positively on temperature, with superionic behavior occurring at high temperatures above 900 K. The diffusivity depends nonmonotonically on the H content, with a maximum at x of 1–2. All hydrides are metallic and elastically stable at the studied thermodynamic conditions. Pressure effects on these properties are also discussed.

2. Computational methods

Ab initio calculations were performed with the Vienna *ab initio* simulation package (VASP)[27] based on DFT using the projector augmented wave method.[28,29] The exchange correlation between electrons can be approximated by generalized gradient approximation (GGA) in the form of Perdew–Burke–Ernzerhof (PBE).[30] The valence electrons of H, Cr, and Zr are $1s^1$, $3s^23p^63d^54s^1$, and $4s^24p^64d^25s^2$, respectively. The plane-wave basis with a cutoff energy of 325 eV was applied, and the convergence criterion for geometric optimization was set to 1×10^{-6} eV/atom for the total energy. For structural relaxation and the calculation of hydrogen diffusion barriers by the climbing-image nudged elastic band (CINEB) method,[31] the sampling k-mesh grid of the Brillouin zone was $5 \times 5 \times 5$. A larger $2 \times 2 \times 2$ supercell containing 64 formula units was sampled at the Γ-point for *ab initio* molecular dynamics (AIMD) simulation. The NVT ensemble uses a Nose–Hoover thermostat with a time step of 1 fs lasting over 20000 steps.

The mean-square displacement (MSD) is calculated using the following formula:

$$\mathrm{MSD} = \frac{1}{N}\left\langle \sum_{i=1}^{N} \left[\boldsymbol{r}_i\left(t'+t\right) - \boldsymbol{r}_i\left(t\right)\right]^2 \right\rangle, \tag{1}$$

where $\boldsymbol{r}_i$ represents the position of the i-th ion at time $t'+t$ and t. N is the number of particles.

The self-Van Hove correlation function is defined to characterize proton dynamics, which can be calculated as follows:[32,33]

$$G_{\mathrm{s}}\left(r,t'\right) = \frac{1}{N}\left\langle \sum_{i=1}^{N} \delta\left(\boldsymbol{r} - \left[\boldsymbol{r}_i\left(t'+t\right) - \boldsymbol{r}_i\left(t\right)\right]\right) \right\rangle, \tag{2}$$

where $\boldsymbol{r}_i$ is the atomic position of the i-th atom, $\boldsymbol{r}$ is a general position in space, and $\delta(\cdot)$ is the Dirac delta function. $G_{\mathrm{s}}(r,t')$ is defined as the probability density of finding a particle at displacement r after time t'.

The elastic modulus was calculated by the Voigt–Reuss–Hill (VRH) averaging method.[34] The crystal orbital Hamilton population (COHP) analysis was performed using the LOBSTER code.[35] All visualizations were performed by VESTA.[36]

3. Results and discussion

The C15 Laves phase of $ZrCr_2$ crystallizes in the *Fd*-3*m* space group (No. 227) with Zr and Cr atoms occupying the 8*a* and 16*d* Wyckoff positions respectively, as shown in Fig. 1(a). Hydrogen atoms absorbed in the $ZrCr_2$ lattice can occupy three types of tetrahedral interstitials: the blue tetrahedron corresponds to the 96*g* site, yellow to 8*b*, and pink to 32*e*. As shown in Fig. 1(b), the occupation of hydrogen atoms on these interstitials significantly expands the lattice volume, with an average hydrogen atomic volume of about 2.85 Å^3 at 0 GPa. All compounds demonstrate a monotonically decreasing volumetric response to applied pressure, consistent with typical elastic compression behavior in crystalline solids. Volume reduction reaches 8.7%–8.9% upon compression to 20 GPa, resulting in a reduction of the nearest distance between interstitial sites by 2.4%–3.5% and a decrease of the hydrogen atomic volume by about 7.4%.

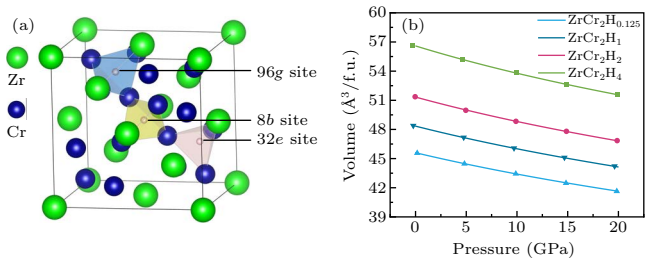


Fig. 1. (a) Crystal structure of the C15 Laves phase $ZrCr_2$, where Zr atoms (green) and Cr atoms (blue) are shown. In the crystal structure, hydrogen preferentially occupies three tetrahedral sites represented by different colors: 96*g*, 8*b*, and 32*e* Wyckoff positions. (b) Pressure-dependent unit cell volume evolution of $ZrCr_2H_x$ with different hydrogen contents.

To probe proton dynamics in metal hydrides, AIMD simulations were carried out over a temperature range of 300–1100 K and pressures of 0–20 GPa. As shown in Fig. 2, the mean square displacement (MSD, $\langle\mu^2\rangle$) data reveal a significant impact of temperature, stoichiometry, and pressure on diffusivity in these hydrides. At 300 K, $\langle\mu^2\rangle$ does not increase significantly with simulation time, yielding a small diffusion coefficient (D) below 10^{-6} cm^2·s^{-1} at 0–20 GPa. As temperature rises, $\langle\mu^2\rangle$ exhibits steeper slopes, signaling enhanced atomic diffusion. At 900 K, the D values reach about 3×10^{-4} cm^2·s^{-1} at 0–20 GPa, which exceeds the threshold for superionic transport in classical liquids (i.e., $D > 10^{-4}$ cm^2·s^{-1}). Notably, the diffusivity does not depend monotonically on hydrogen concentration. For instance, $ZrCr_2H_4$ typically has slopes of $\langle\mu^2\rangle$ less steep than those of $ZrCr_2H_1$ and $ZrCr_2H_2$ at comparable temperature and pressure, suggesting that reduced vacancy concentration impedes hydrogen migration. Compression induces appreciable lattice contraction in all these hydrides. Depending on composition, lattice contraction may exert opposite effects on diffusivity. Specifically, it usually suppresses diffusivity at higher H concentration (e.g., $ZrCr_2H_4$ at 700 K) but can also enhance it

at lower H concentration (e.g., $ZrCr_2H_{0.125}$ at 700 K). These findings reveal strong competition between stoichiometry and pressure effects on diffusivity in the $ZrCr_2H_x$ system.

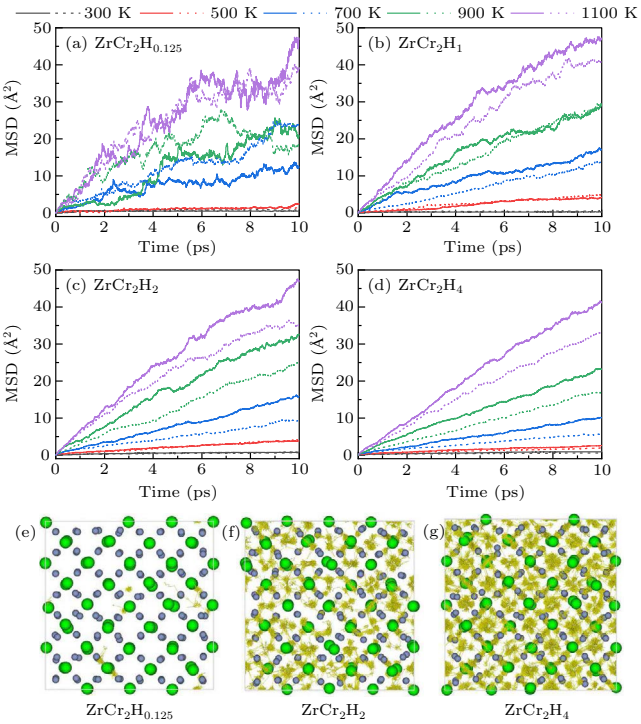


Fig. 2. Hydrogen diffusion characteristics in $ZrCr_2H_x$ with varying stoichiometry: (a) $ZrCr_2H_{0.125}$, (b) $ZrCr_2H_1$, (c) $ZrCr_2H_2$, (d) $ZrCr_2H_4$. Solid (0 GPa) and dashed (20 GPa) lines denote pressure conditions, with temperatures color-coded in the top legend: black (300 K), red (500 K), blue (700 K), green (900 K), and purple (1100 K). (e)–(g) Trajectories of H atoms at 500 K are represented by yellow lines within the crystal lattice. Zr and Cr atoms are depicted as green and blue spheres, respectively.

We analyze the radial distribution function (RDF, $g(r)$) of $ZrCr_2H_x$ ($x = 0.125$ and 4) at 300 K and 900 K to elucidate the structural characteristics of dynamic hydrogen configurations in both normal and superionic states. As shown in Fig. 3, temperature governs both the shape and peak positions of $g(r)$ in both hydrides, and clearly shows more significant effects in $ZrCr_2H_{0.125}$ compared to $ZrCr_2H_4$. Thermal activation from 300 to 900 K shifts the first peak by approximately 3.5 Å from about 5.5 Å to 2 Å in $ZrCr_2H_{0.125}$, whereas it only slightly broadens the peaks in $ZrCr_2H_4$. Pressure effects are also more pronounced in the former than in the latter, but the overall effect is much less than that of temperature. For $ZrCr_2H_4$, the first coordination shell has the peak position located at 2.1 Å with a full width at half maximum of 0.34 Å at 0 GPa. It is found that dynamic hydrogen configurations permit H–H separations as low as 1.41 Å, violating the Switendick criterion (2.1 Å threshold), reminiscent of the ultra-short H–H separation (1.6 Å) observed in $ZrV_2H_{4-\delta}$ under ambient conditions.[24] For $ZrV_2H_{4-\delta}$, this phenomenon was rationalized by the contribution of configurational entropy at finite temperatures, which allows short H–H distances to emerge in thermodynamic equilibrium.[24] Here, our molecular dynamics simulations on $ZrCr_2H_4$ reveal that this is more of a transient dynamic phenomenon involving diffusion of hydrogen atoms. These findings suggest that dynamic hydrogen networks in 'C15-type' hydrides may generally violate the Switendick criterion.

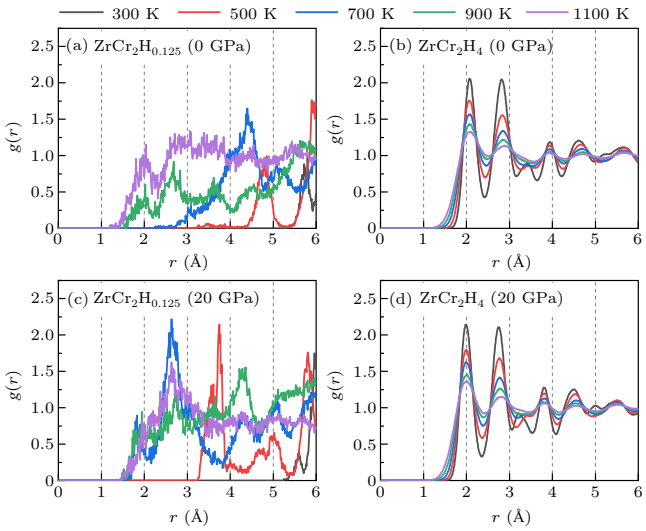


Fig. 3. Comparison of radial distribution functions (RDFs) for (a) $ZrCr_2H_{0.125}$ at 0 GPa, (b) $ZrCr_2H_4$ at 0 GPa, (c) $ZrCr_2H_{0.125}$ at 20 GPa, and (d) $ZrCr_2H_4$ at 20 GPa. Temperature progression is color-coded: black (300 K), red (500 K), blue (700 K), green (900 K), and purple (1100 K).

Within the $ZrCr_2$ lattice, the spatial distribution of the three types of interstitial sites (i.e., *g*, *e*, and *b*) dictates that the *g* and *e* sites form a three-dimensional connected main network, while the *b* sites are weakly connected to the main network as locally bridging points between *e* sites. These junctions provide three basic diffusion pathways: *g*–*g*, *g*–*e*, and *e*–*b*, with characteristic spacings of 1.15 Å, 1.27 Å, and 1.32 Å in the $ZrCr_2$ lattice with *a* of 7.683 Å, which is equal to that of $ZrCr_2H_4$ at 0 GPa. Since the next-nearest *g*–*g* distance (1.33 Å) is close to that of *e*–*b*, it is also analyzed as an additional basic pathway for comparison (denoted as *g*–*g*′). According to the equation of state of $ZrCr_2H_x$, these interatomic spacings decrease with lattice contraction, driven by either H concentration depletion or increased pressure.

Taking $ZrCr_2H_4$ as an example, we analyze hydrogen diffusion behavior in this class of hydrides using self-Van Hove correlation functions (G_s). As illustrated in Fig. 4(a), a distinct density distribution emerges around a radial distance of 3 Å, indicating the presence of long-range diffusion within 10 ps under conditions of 300 K and 0 GPa. Further comparison with the G_s pattern at 20 GPa (Fig. 4(c)) suggests that lattice contraction suppresses long-range diffusion at 300 K.

Notably, the linkage of the *g*–*g* paths forms localized hexagonal rings, and one- and two-step hopping within them correspond to hopping distances of 1.15 Å and 1.98 Å, respectively. The latter is comparable to those of two-step hopping through the *g*–*g*–*e* (1.9 Å), *g*–*e*–*g* (2.1 Å), *g*–*e*–*b* (2.1 Å), and *g*′–*e*–*g* (2.1 Å) pathways. Therefore, the density distribution around 2.0 Å may indicate the activation of either intra-ring

diffusion or inter-ring diffusion. In any case, the much earlier and denser distributions around 1.2 Å suggest that H atoms can be trapped for a considerable time after the initial hopping.

Previously, a dual-path diffusion model involving intra-ring and inter-ring diffusion was proposed for $TiCr_2H_x$.[37] Compared to this model, the present study further identifies potential two-step hopping pathways, providing a more comprehensive understanding of hydrogen diffusion complexity in the C15 structure. Thermal activation to 900 K leads to faster long-range diffusion with a significant reduction in trapping time at both 0 GPa and 20 GPa, which is consistent with the superionic nature predicted by MSD analysis under comparable thermodynamic conditions.

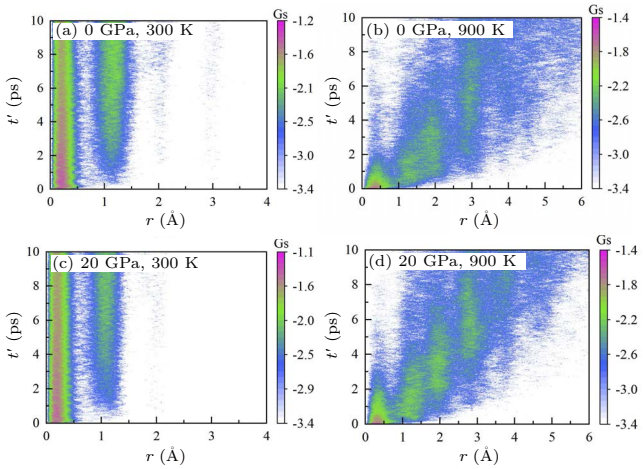


Fig. 4. Self-Van Hove correlation functions (G_s) for hydrogen diffusion in $ZrCr_2H_4$ at different pressures and temperatures. (a) 0 GPa, 300 K, (b) 0 GPa, 900 K, (c) 20 GPa, 300 K, and (d) 20 GPa, 900 K.

We study the activation barriers of four basic diffusion pathways (e.g. *g*–*g*, *g*–*g*′, *g*–*e*, and *e*–*b*) by the CINEB method at pressures of 0 GPa and 20 GPa. As shown in Fig. 5, the *g*–*g* and *e*–*b* pathways are the least pressure-sensitive and most pressure-sensitive pathways, respectively. Their barrier heights increase by less than 1% and over 35% as pressure rises from 0 to 20 GPa. Meanwhile, the *g*–*g*′ and *g*–*e* pathways exhibit moderate pressure sensitivity while maintaining relatively consistent barrier heights, which increase by about 10% under the same compression (0–20 GPa). Pressure-induced lattice contraction usually enhances metal–hydrogen orbital interactions, thereby elevating diffusion energy barriers. The case of the *g*–*g* pathway emphasizes the complex dependence of energy barriers on atomic environments. The barrier heights exhibit a trend of g–$g' \approx g$–$e < g$–$g < e$–b at both 0 GPa and 20 GPa, with *e*–*b* (0.34–0.46 eV) exceeding the others by about 40%–100% at 0–20 GPa. This result is consistent with DFT binding-energy analysis of $TiCr_2H_x$, which identified the *b* site as the least favorable site for hydrogen occupation.[38] The relatively lower barriers of the *g*–*g*′, *g*–*e*, and *g*–*g* pathways (0.20–0.23 eV) suggest that they are major contributors to long-range diffusion. This scenario is consistent with the MD simulations. For example, we retrieve atomic trajectories associated with two-step hopping from MD simulations of $ZrCr_2H_4$ at 300 K and 0 GPa (Fig. S1), and find direct evidence of hydrogen diffusion through the *g*–*g*′–*e*, *g*′–*g*′–*g*, and *g*–*e*–*g*′ pathways.

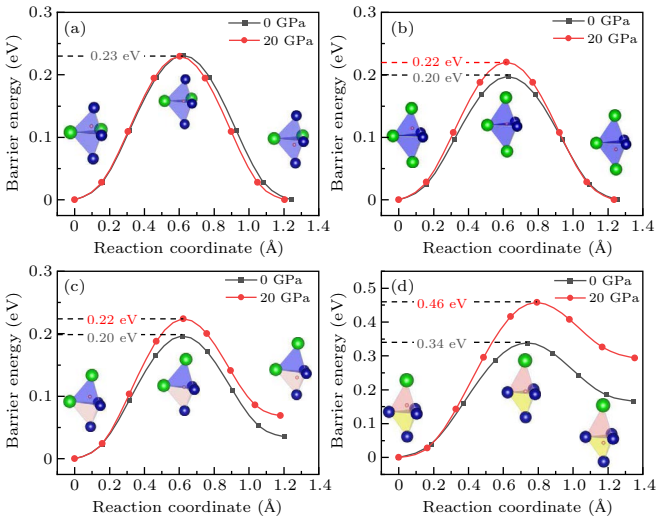


Fig. 5. Diffusion pathways for hydrogen migration in $ZrCr_2$ interstitial sites: (a) *g*–*g*, (b) *g*–*g*′, (c) *g*–*b*, and (d) *e*–*b*. The green, yellow, and pink spheres in each inset represent Zr, Cr, and H atoms, respectively. The tetrahedra Zr_2Cr_2, $ZrCr_3$, and Cr_4, composed of Zr and Cr atoms, are shown in blue, pink, and yellow, respectively.

Elastic constants are fundamental parameters that define the mechanical behavior of a material. In cubic crystal systems, there are three independent elastic constants C_{11}, C_{12}, and C_{44}, which describe the mechanical response to uniaxial compression, shear deformation coupled with hydrostatic pressure, and shear deformation along non-principal axes, respectively. Based on the stress–strain relationships obtained in AIMD calculations, we derive the elastic constants of $ZrCr_2H_x$ ($x = 0.125$, 1, and 2) at 0 GPa and 300 K, as shown in Table 1. As x increases from 0.125 to 2, C_{11} decreases by 6%, C_{12} decreases by 15%, and C_{44} increases by 34%. The elastic constants of $ZrCr_2H_4$ at 0–20 GPa and 300–900 K were also calculated. Compared to $ZrCr_2H_2$, $ZrCr_2H_4$ shows smaller C_{11} and C_{44} but larger C_{12} under the same thermodynamic conditions, indicating that elasticity does not depend monotonically on H concentration. We further analyze the temperature and pressure effects on these elastic constants in $ZrCr_2H_4$. At 0–20 GPa, an increase in temperature leads to an increase in C_{11} but a decrease in C_{12} and C_{44}, whereas increasing pressure results in a uniform increase in these elastic constants.

According to Born's stability criteria, the mechanical stability of cubic crystals under equilibrium conditions is ensured by satisfying three conditions: $C_{11} + 2C_{12} > 0$, $C_{11} - C_{12} > 0$, and $C_{44} > 0$, associated with volumetric, tetragonal shear, and transverse shear stabilities, respectively. It is found that $ZrCr_2H_x$ ($x = 0.125$, 1, 2, and 4) satisfies these criteria at 0 GPa and the temperatures studied. Under compression, mod-

ified criteria should be adopted to include the effects of external pressure (p), i.e., $C_{11}+2C_{12}+p>0$, $C_{11}-C_{12}-2p>0$, and $C_{44}-p>0$. As shown in Table 1, $ZrCr_2H_4$ also satisfies these criteria at 20 GPa and 300–900 K. The results suggest that $ZrCr_2H_x$ is mechanically stable at 0–20 GPa and 300–900 K, although significant hydrogen diffusion may occur. In addition, the bulk modulus (B), shear modulus (G), and Poisson's ratio (ν) were calculated using the Voigt–Reuss–Hill averaging method, and the results are shown in Table 1. The B/G and ν values are greater than 1.75 and 0.25, respectively, indicating good ductility of $ZrCr_2H_x$, according to Pugh's criterion and standard interpretations of Poisson's ratio.

Table 1. AIMD simulated elastic constants, bulk modulus (B), shear modulus (G), and Poisson's ratio (ν) of $ZrCr_2H_x$ at different temperatures and pressures.

P (GPa)	T (K)	Composition	C_{11}	C_{12}	C_{44}	B (GPa)	G (GPa)	ν
0	300	$ZrCr_2H_{0.125}$	226.2	157.9	47.2	180.6	42.0	0.39
0	300	$ZrCr_2H_1$	221.7	136.6	58.3	164.9	52.0	0.36
0	300	$ZrCr_2H_2$	212.3	133.5	63.3	159.8	53.7	0.35
0	300	$ZrCr_2H_4$	179.7	147.1	53.6	158.0	38.7	0.39
20	300	$ZrCr_2H_4$	277.2	208.0	65.2	231.1	53.0	0.39
0	900	$ZrCr_2H_4$	200.7	127.7	42.6	152.0	40.2	0.38
20	900	$ZrCr_2H_4$	292.1	201.4	45.3	231.7	45.3	0.41

To explore the electronic properties of this class of hydrides, we calculated the total and projected density of states (DOSs) for $ZrCr_2H_4$ at 300 K and 0 GPa by averaging over DOSs from 20 MD configurations. As shown in Fig. 6(a), the low-energy region (below −4 eV) shows strong H character, while the high-energy region (above −4 eV) contains more pronounced Zr and Cr contributions. Notably, H dominates the DOS in the energy range of −10.5 eV to −9.5 eV, suggesting the formation of localized electronic states associated with nearest H–H pairs. From −9.5 eV to −4 eV, hybridization among H, Zr, and Cr orbitals is observed, confirming chemical bonding between H atoms and the $ZrCr_2$ host lattice. From −4 eV to 0 eV, the DOS is primarily composed of strongly hybridized Cr-d and Zr-d states, with minor contributions from Cr-p, Zr-p, and H-s states.

To further elucidate the bonding characteristics, we also analyzed the integrated COHP (i.e., ICOHP) for distinct atomic pairs. As shown in Fig. 6(b), smaller atomic separations generally result in larger −ICOHP values, indicating higher covalency of the pairwise interactions. In terms of sensitivity of ICOHP to atomic separation, the interactions can be roughly classified into three categories: (i) H–H, with low sensitivity; (ii) Cr–H, Zr–H, Cr–Zr, and Zr–Zr, with moderate sensitivity; (iii) Cr–Cr, with high sensitivity, with −ICOHP values spanning the ranges of 0–0.25, 0.25–2.0, and 0.5–4.0, respectively. The results reflect a complex electronic structure in $ZrCr_2H_4$ influenced by both covalent and metallic interactions.

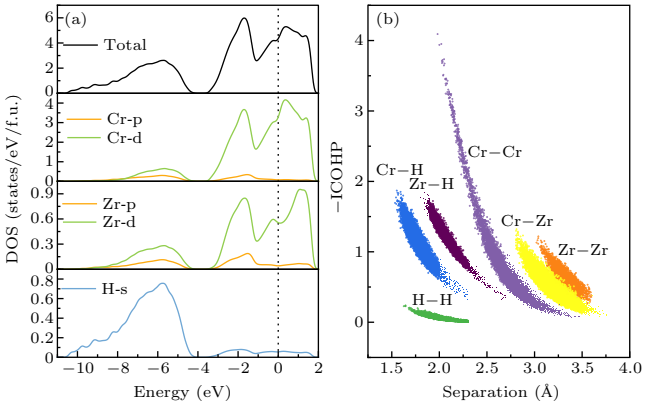


Fig. 6. Electronic structure analysis from molecular dynamics trajectory sampling: (a) total and projected DOS of $ZrCr_2H_4$ at 300 K and 0 GPa; (b) integrated crystal orbital Hamilton population (−ICOHP) for different atomic pairs.

In summary, we investigated the dynamic, mechanical, and electronic properties of the C15-type $ZrCr_2H_x$ ($0<x<4$) hydrides at pressures ranging from 0 to 20 GPa using first-principles calculations. We found that interstitial hydrogen induces lattice expansion, resulting in an average volume change of 2.75 $Å^3\cdot atom^{-1}$. In all these hydrides, thermal activation at 900 K leads to superionic states with proton diffusion coefficients up to 10^{-4} $cm^2\cdot s^{-1}$. At lower temperatures, pressure competes with H concentration in determining diffusivity. Proton diffusion significantly increases the probability of neighboring interstitial sites being occupied, resulting in H–H separations of less than 2.1 Å, which violate the Switendick criterion. A detailed analysis of both activation barriers and atomic trajectories reveals that protons mainly diffuse through the interstitial network composed of g and e sites, while they rarely occupy b sites due to the high energy barrier. At 0 GPa and 300 K, all hydrides are mechanically stable, and increasing hydrogen concentration leads to a monotonic decrease in the elastic constant C_{11} and the bulk modulus B. For $ZrCr_2H_4$, a high hydrogen concentration results in a clear contribution of H s orbitals to metallicity. This suggests that C15-type metal hydrides have great potential to be developed into 'H-rich' superconductors at low pressures.

Acknowledgment

Project supported by the National Natural Science Foundation of China (Grant No. 12474223).

References

[1] Drozdov A P, Kong P P, Minkov V S, Besedin S P, Kuzovnikov M A, Mozaffari S, Balicas L, Balakirev F F, Graf D E, Prakapenka V B, Greenberg E, Knyazev D A, Tkacz M and Eremets M I 2019 *Nature* **569** 528

[2] Somayazulu M, Ahart M, Mishra A K, Geballe Z M, Baldini M, Meng Y, Struzhkin V V and Hemley R J 2019 *Phys. Rev. Lett.* **122** 027001

[3] Wang H, Tse J S, Tanaka K, Iitaka T and Ma Y M 2012 *Proc. Nat. Acad. Sci. USA* **109** 6463

[4] Liu H Y, Naumov I I, Hoffmann R, Ashcroft N W and Hemley R J 2017 *Proc. Nat. Acad. Sci. USA* **114** 6990

[5] Kong P P, Minkov V S, Kuzovnikov M A, Drozdov A P, Besedin S P, Mozaffari S, Balicas L, Balakirev F F, Prakapenka V B, Chariton S, Knyazev D A, Greenberg E and Eremets M I 2021 *Nat. Commun.* **12** 5075

[6] Ma L, Wang K, Xie Y, Yang X, Wang Y Y, Zhou M, Liu H Y, Yu X H, Zhao Y S, Wang H B, Liu G T and Ma Y M 2022 *Phys. Rev. Lett.* **128** 167001

[7] Semenok D V, Kvashnin A G, Ivanova A G, Svitlyk V, Fominski V Y, Sadakov A V, Sobolevskiy O A, Pudalov V M, Troyan I A and Oganov A R 2020 *Mater. Today* **33** 36

[8] Zhang Z H, Cui T, Hutcheon M J, Shipley A M, Song H, Du M Y, Kresin V Z, Duan D F, Pickard C J and Yao Y S 2022 *Phys. Rev. Lett.* **128** 047001

[9] Cerqueira T F T, Fang Y W, Errea I, Sanna A and Marques M A L 2024 *Adv. Funct. Mater.* **34** 2404043

[10] Jiang B W, Luo X S, Sun Y, Zhong X, Lv J, Xie Y, Ma Y M and Liu H Y 2025 *Phys. Rev. B* **111** 054505

[11] Dolui K, Conway L J, Heil C, Strobel T A, Prasankumar R P and Pickard C J 2024 *Phys. Rev. Lett.* **132** 166001

[12] Yu F F, Xiang X, Xu C H, Zu X T and Hu S L 2024 *Int. J. Hydrogen Energy* **81** 1288

[13] Zhu B S, Shao D X, Pei C Y, Wang Q, Wu J F and Qi Y P 2025 *Phys. Rev. B* **111** 054517

[14] Gu T T, Cui W W, Hao J, Shi J M, Durajski A P, Liu H Y and Li Y W 2024 *Phys. Rev. B* **110** 064105

[15] He X L, Zhao W B, Xie Y, Hermann A, Hemley R J, Liu H Y and Ma Y M 2024 *Proc. Nat. Acad. Sci. USA* **121** e2401840121

[16] Zhang K X, Yu J K, Zhang Y C, Guo J N, Wang Y L, Jiang C, Huang X L and Cui T 2025 *J. Am. Chem. Soc.* **147** 11879

[17] Song X X, Hao X K, Wei X D, He X L, Liu H Y, Ma L, Liu G T, Wang H B, Niu J Y, Wang S J, Qi Y P, Liu Z Y, Hu W T, Xu B, Wang L, Gao G Y and Tian Y J 2024 *J. Am. Chem. Soc.* **146** 13797

[18] Chen W H, Huang X L, Semenok D V, Chen S, Zhou D, Zhang K X, Oganov A R and Cui T 2023 *Nat. Commun.* **14** 2660

[19] Bi J K, Nakamoto Y, Zhang P Y, Shimizu K, Zou B, Liu H Y, Zhou M, Liu G T, Wang H B and Ma Y M 2022 *Nat. Commun.* **13** 5952

[20] Radaković J, Belošević-Čavor J and Koteski V 2013 *Int. J. Hydrogen Energy* **38** 9229

[21] Stein F and Leineweber A 2021 *J. Mater. Sci.* **56** 5321

[22] Switendick A C 1979 *Z. Phys. Chem. Neue Folge* **117** 89

[23] Rao B K and Jena P 1985 *Phys. Rev. B* **31** 6726

[24] Borgschulte A, Terreni J, Billeter E, Daemen L, Cheng Y, Pandey A, Łodziana Z, Hemley R J and Ramirez-Cuesta A J 2020 *Proc. Nat. Acad. Sci. USA* **117** 4021

[25] Shen H, Zhang J X, Paul Boncour V, Li P, Li Z, Wu Y and Jiang L 2024 *J. Rare Earths* **42** 803

[26] Budziak A and Szafraniec J 2023 *Energies* **16** 7383

[27] Kresse G and Furthmüller J 1996 *Phys. Rev. B* **54** 11169

[28] Kresse G and Joubert D 1999 *Phys. Rev. B* **59** 1758

[29] Blöchl P E 1994 *Phys. Rev. B* **50** 17953

[30] Perdew J P, Burke K and Ernzerhof M 1996 *Phys. Rev. Lett.* **77** 3865

[31] Henkelman G, Uberuaga B P and Jónsson H 2000 *J. Chem. Phys.* **113** 9901

[32] Treffenstädt L L, Schindler T and Schmidt M 2022 *SciPost Phys.* **12** 133

[33] Haddadian E J, Zhang H, Freed K F and Douglas J F 2017 *Sci. Rep.* **7** 41671

[34] Hill R 1952 *Proc. Phys. Soc. A* **65** 349

[35] Deringer V L, Tchougréeff A L and Dronskowski R 2011 *J. Phys. Chem. A* **115** 5461

[36] Momma K and Izumi F 2011 *J. Appl. Crystallogr.* **44** 1272

[37] Miwa K and Asahi R 2019 *Int. J. Hydrogen Energy* **44** 23708

[38] Kumar P, Kormann F, Grabowski B and Ikeda Y 2019 *Acta Mater.* **297** 121319